Research
Material Science and Engineering—Article

Sodium Nitrate Passivation as a Novel Insulation Technology for Soft Magnetic Composites

Mi Yan [a,*], Qiming Chen [a], Dong Liu [a,b], Chen Wu [a,*], Jian Wang [c]

[a] *State Key Laboratory of Silicon Materials, School of Materials Science and Engineering, Zhejiang University, Hangzhou 310027, China*
[b] *School of Chemical Engineering, Shandong University of Technology, Zibo 255049, China*
[c] *National Institute for Materials Science, Tsukuba 305-0047, Japan*

A B S T R A C T

Sodium nitrate passivation has been developed as a new insulation technology for the production of FeSiAl soft magnetic composites (SMCs). In this work, the evolution of coating layers grown at different pH values is investigated involving analyses on their composition and microstructure. An insulation coating obtained using an acidic $NaNO_3$ solution is found to contain Fe_2O_3, SiO_2, Al_2O_3, and $AlO(OH)$. The Fe_2O_3 transforms into Fe_3O_4 with weakened oxidizability of the NO_3^- at an elevated pH, whereas an alkaline $NaNO_3$ solution leads to the production of Al_2O_3, $AlO(OH)$, and SiO_2. Such growth is explained from both thermodynamic and kinetic perspectives and is correlated to the soft magnetic properties of the FeSiAl SMCs. Under tuned passivation conditions, optimal performance with an effective permeability of 97.2 and a core loss of 296.4 mW·cm^{-3} is achieved at 50 kHz and 100 mT.

© 2022 THE AUTHORS. Published by Elsevier LTD on behalf of Chinese Academy of Engineering and Higher Education Press Limited Company. This is an open access article under the CC BY-NC-ND license (http://creativecommons.org/licenses/by-nc-nd/4.0/).

1. Introduction

Soft magnetic materials are of significant importance in electromagnetic conversion applications [1]. Compared with ferrites, soft magnetic alloys exhibit higher saturation magnetization and permeability, but their applications at high frequencies are restricted due to their inevitable high eddy current losses. To tackle this issue, various efforts have been dedicated to the development of soft magnetic composites (SMCs) which are composed of metallic magnetic powders embedded in an insulation matrix [2,3]. The key to obtaining such a structure lies in the insulation coating of the magnetic powders, which is indispensable for increasing the electrical resistivity and suppressing the eddy current loss [4]. The formation of this coating can be classified into two categories, depending on whether or not the elements of the metallic powders are involved in the insulation process. In the first category, sol–gel [5–7], precipitation [8], and so forth are used to obtain coatings such as Al_2O_3, MgO, and SiO_2 with no participation of the powder elements. The coatings fabricated by such methods exhibit weak adhesion and tend to crack during compaction, resulting in a deteriorated performance. In the second category, direct reactions of the metal elements with passivation solutions such as acids and oxidizing salts are used [9,10]. Compared with the use of sol–gel and precipitation, the coatings formed by *in situ* reactions between the powders and oxidation solutions exhibit enhanced adhesiveness to the powders and compatibility for industrialization. For example, phosphatization is the method most widely used to generate phosphate insulation layers [11,12]. However, the resultant phosphates tend to decompose at temperatures above 600 °C [13], which limits the subsequent annealing temperature for complete stress relaxation. Consequently, there is an urgent need to develop new insulation technology to form thin and complete passivation layers with satisfactory adhesion and thermal stability. Furthermore, accurate control of the reaction conditions during wet chemical passivation based on an in-depth understanding of the kinetic and thermodynamic mechanisms is required.

In this study, based on the most frequently used FeSiAl soft magnetic alloy with high permeability, low magnetostriction, and anisotropy, a $NaNO_3$ passivation technology is developed with both controllability and compatibility with existing industrial setups. The evolution of the composition and microstructure of the coatings under different conditions is investigated based on delicate microscopic observations and kinetic and thermodynamic analyses. The correlation between the evolution of the coating layer and the magnetic performance is also revealed.

* Corresponding authors.
 E-mail addresses: mse_yanmi@zju.edu.cn (M. Yan), chen_wu@zju.edu.cn (C. Wu).

2. Experimental methods

NaNO$_3$ solution (10.0 wt%–30.0 wt%, 30.0 mL) was used as the passivation solution at a pH ranging from 2 to 8, adjusted by means of a CH$_3$COOH and CH$_3$COONa buffer solution. The NaNO$_3$, CH$_3$COOH, and CH$_3$COONa were all purchased from Sinopharm Chemical Reagents Co., Ltd., China. Fe–9.6 wt% Si–5.4 wt% Al powders (20.0 g) commercially available from Changsha Tijo Metal Materials Co., Ltd., China, with two different sizes were mixed (30 wt% at 50 μm and 70 wt% at 75 μm), prior to being dispersed into 30.0 mL of NaNO$_3$ solution under constant stirring for 10 min at 25 °C. The as-coated powders were then cleaned in anhydrous ethanol (Sinopharm Chemical Reagents Co., Ltd.) and vacuum dried at 80 °C, followed by mixing with zinc stearate (0.5 wt%; Shanghai Macklin Biochemical Co., Ltd., China) as a lubricant. The composite powders were cold-compacted into toroidal cores (outer diameter = 23.6 mm, inner diameter = 14.4 mm, and thickness = 7.0 mm) at 1900 MPa. Finally, the compacted samples were subjected to annealing at 700 °C for 1 h under the protection of argon for stress relaxation.

The powder morphology was examined through scanning electron microscopy (SEM; Hitachi S-4800, Hitachi, Ltd., Japan). The chemical structures of the coatings were studied by Fourier-transform infrared (FTIR) spectroscopy (Nicolet 5700, Thermo Fisher Scientific Inc., USA) and X-ray photoelectron spectroscopy (XPS; ESCALAB 250Xi, Thermo Fisher Scientific Inc.). The composition and detailed microstructure were characterized by transmission electron microscopy (TEM; Titan G2 80–200, FEI Company Inc., USA) with selected-area electron diffraction (SAED) and energy-dispersive X-ray spectroscopy (EDS). Fig. S1 in Appendix A illustrates the preparation method used for the TEM samples with a focused ion beam (FIB). The density and open porosity of the cores were measured based on the Archimedes principle; detailed calculations are provided in the Supplementary Information in Appendix A. The electrical resistivity of the cores was examined using the four-point probe method. The core loss and effective permeability were investigated using an auto testing system (MATS-2010SA, Hunan Linkjoin Technology Co., Ltd., China) in the frequency range of 25–175 kHz at 100 mT.

3. Results and discussion

3.1. Magnetic properties of the composites

The concentration of the NaNO$_3$ passivation solution was varied from 10 wt% to 30 wt%; its effects on the core loss P_{cv} and effective permeability μ_e are shown in Fig. S2 in Appendix A, where 20 wt% NaNO$_3$ passivation gives rise to the formation of thin and complete insulation layers for enhanced performance. Next, the pH of the NaNO$_3$ solution with a concentration of 20 wt% was adjusted using a CH$_3$COOH and CH$_3$COONa buffer solution. Fig. 1 shows the effects of varying the pH value of the NaNO$_3$ solution from 2 to 8 on the P_{cv} and μ_e of the SMCs at a concentration of 20 wt%. Detailed values of the P_{cv} and μ_e obtained at 50 kHz, as well as the measured density, porosity, and resistivity, are summarized in Table 1. The P_{cv} shows a decreasing trend as the pH value is increased to 5 (296.4 mW·cm^{-3}), followed by an increment to 660.2 mW·cm^{-3} at pH 8, as shown in the inset of Fig. 1(a).

As the pH is increased from 2 to 4, the μ_e decreases from 143.4 to 82.5 (Fig. 1(b)). A further increase in the pH monotonically increases the μ_e to 157.6 at pH 8. Optimized magnetic performance (P_{cv} = 296.4 mW·cm^{-3} and μ_e = 97.2) is achieved at pH 5. Further discussion on the changes in the magnetic properties will be provided in subsequent sections. Table S1 in Appendix A compares the observed core loss and permeability with those of previously
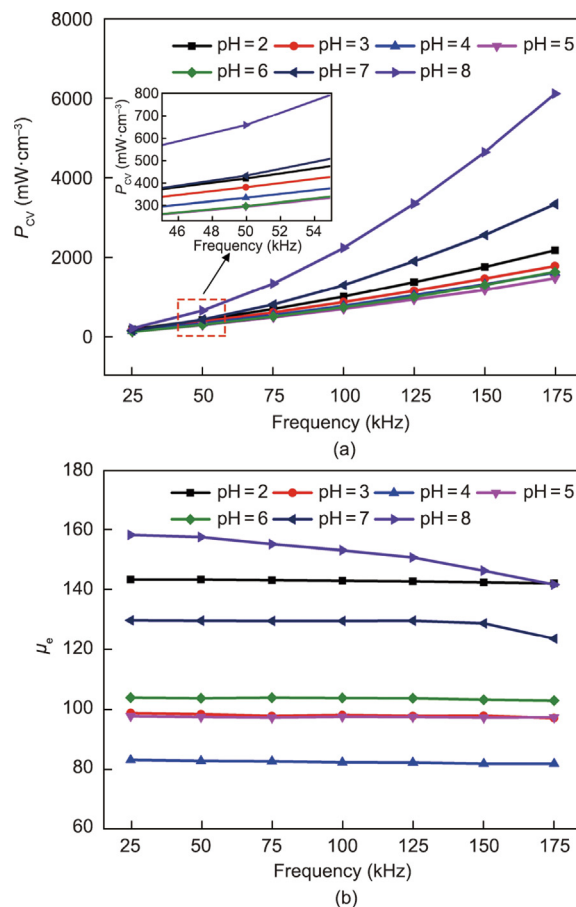

Fig. 1. (a) Core loss (P_{cv}) and (b) effective permeability (μ_e) against frequency, taken from samples passivated by 20 wt% NaNO$_3$ at different pH values.

reported FeSiAl SMCs prepared via other insulation methods and indicates that the SMCs fabricated here exhibit advantageous comprehensive alternating current (AC) magnetic properties.

3.2. Insulation coating characterizations

Fig. 2 shows SEM images of the FeSiAl powders passivated with NaNO$_3$ solution at pH values of 2, 5, and 8. A discontinuous insulation coating can be observed for the sample at pH 2, which may be due to strong surface reactions (Figs. 2(a) and (b)). The FeSiAl powder exhibits a relatively smooth surface (Fig. 2(c)) at pH 5, with a uniform insulation coating, as shown in the enlarged image in Fig. 2(d). Further increasing the pH to 8 results in incomplete insulation, as indicated by the square region in Fig. 2(e), which is enlarged in Fig. 2(f).

To reveal the insulation evolution, FTIR spectra were obtained for the FeSiAl powders before and after passivation at different pH values (Fig. 3). For all the samples, the strong absorption peaks around 1630 and 3430 cm^{-1} correspond to the stretching bands of the adsorbed water [14]. For the uncoated FeSiAl, the band at 470 cm^{-1} originates from Si–O–Si stretching [15], and the peaks at 490 and 580 cm^{-1} can be assigned to the Fe–O bond [16,17]. The stretching vibrations of Al–O and Al–O–Al contribute to the peaks at 619 and 723 cm^{-1} [18]. The coexistence of Fe–O, Al–O, and Si–O suggests surface oxidation of the raw powders. For the FeSiAl powders passivated at pH 2, additional absorption bands are observed around 1430 and 1590 cm^{-1}, which originate from the symmetric and asymmetric stretching modes for COO$^-$

Table 1
Core loss (P_{cv}), effective permeability (μ_e), density, porosity, and electrical resistivity of the composites at different pH values.

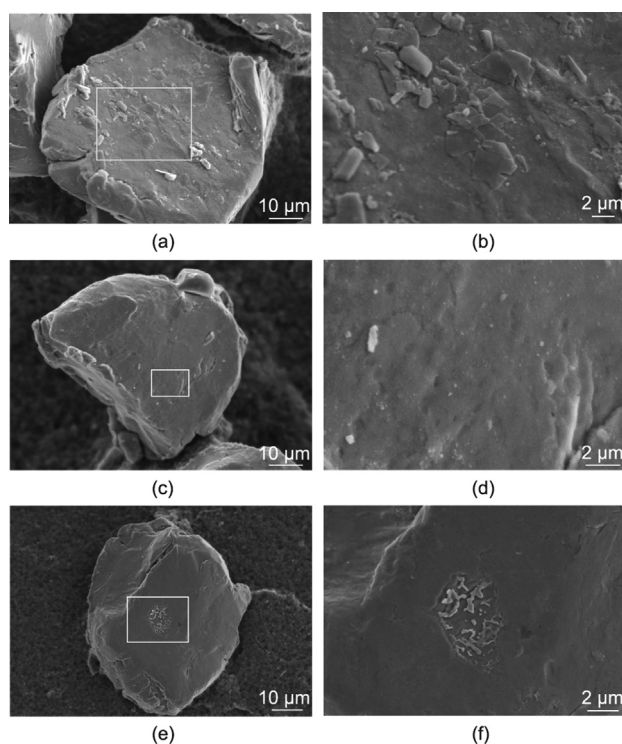| pH value	P_{cv} (mW·cm^{-3})	μ_e	Density (g·cm^{-3})	Porosity (%)	Electrical resistivity (Ω·cm)
2	421.4	143.4	6.17	7.84	0.96
3	382.4	98.2	6.11	8.41	2.12
4	335.7	82.5	6.01	9.22	5.21
5	296.4	97.2	6.10	8.36	8.23
6	299.1	103.5	6.13	8.12	7.86
7	433.9	129.6	6.16	7.49	4.52
8	660.2	157.6	6.21	6.58	0.16

Fig. 2. SEM images of FeSiAl powders passivated by NaNO$_3$ at a pH of (a, b) 2, (c, d) 5, and (e, f) 8. Enlarged images from the rectangles indicated in (a), (c), and (e) are shown in (b), (d), and (f).

[19,20] due to the large concentration of CH$_3$COOH in the solution. A distinctive band also appears at around 1360 cm^{-1} for Fe–OH [21,22], together with Al–OH absorption at 1050 and 1090 cm^{-1} [23–25]. When the pH of the NaNO$_3$ solution is increased to 5, the intensity of the Fe–OH band is significantly strengthened and the Al–OH bands slightly increase, which can be attributed to the enhanced precipitation of hydroxides such as Fe(OH)$_3$ and Al (OH)$_3$ [26–28]. At pH 8, the band corresponding to Fe–OH almost disappears, since the Fe tends not to react with NO$_3^-$ under alkaline conditions. Relatively weak bands for Al–OH are observed, which may be attributed to the growth of a thinner coating. For the sample fabricated at pH 5, the Fe–OH band almost disappears after annealing at 700 °C, while the Fe–O and Al–O bands are enhanced, indicating that the hydroxides decompose to form the corresponding oxides, while residual Al–OH bands remain due to the partial decomposition of the aluminum hydroxide.

XPS characterization was carried out for the powders passivated by NaNO$_3$ at different pH values after annealing at 700 °C. Fig. S3 in Appendix A shows the survey spectra containing the Fe, Al, Si, and O peaks for all samples. Due to the high reactivity of the Al, it accounts for a consideration proportion of the coating layer. With increased pH, the relative Fe 2p peak intensity decreases while

the Al 2p peak increases, indicating that the Fe is less likely to be oxidized in an alkaline environment while the Al follows the opposite trend. Fig. 4(a) shows a detailed Fe 2p spectrum taken from the sample passivated at pH 2; it contains Fe^0 (706.2 eV) and Fe^{3+} (710.7 eV) peaks [29,30], as well as satellite peaks at 718.3 and 732.4 eV, which are characteristic for Fe$_2$O$_3$ [31]. In Fig. 4(b), two main peaks for Al^{3+} (74.3 eV) and Al^0 (72.9 eV) [32] can be observed. The detection of Fe^0 and Al^0 indicates a thin insulation coating. The spectrum in Fig. 4(c) contains Si^0 (98.4 eV) and Si^{4+} (102.1 eV), which can be assigned to Si and SiO$_2$ [33,34]. The O 1s peak in Fig. 4(d) can be fitted with four components at 529.4, 530.3, 531.2, and 532.5 eV, which can be assigned to Fe^{3+}, Al^{3+}, OH$^-$, and Si^{4+}, respectively [31–33]. Thus, the passivation layer with NaNO$_3$ at pH 2 mainly consists of Fe$_2$O$_3$, Al$_2$O$_3$, SiO$_2$, and hydroxides.

When the pH is raised to 5, the Fe 2p spectrum, shown in Fig. 4(e), consists of the Fe^0 (706.9 eV), Fe^{2+}(709.2 eV), and Fe^{3+} (710.9 eV) peaks. The ratio of Fe^{2+} to Fe^{3+} is less than 1:2, indicating the coexistence of Fe$_2$O$_3$ and Fe$_3$O$_4$. Similarly, the Al spectrum shown in Fig. 4(f) is resolved into Al^{3+} and Al^0, while the Si spectrum shown in Fig. 4(g) contains the Si^{4+} and Si^0 peaks. The O 1s peak in Fig. 4(h) is fitted with five components located at 529.1, 529.9, 530.8, 531.7, and 532.7 eV, which correspond to Fe^{2+}, Fe^{3+}, Al^{3+}, OH$^-$, and Si^{4+}, respectively. Thus, the insulation coating obtained by means of NaNO$_3$ at pH 5 mainly consists of Fe$_2$O$_3$, Fe$_3$O$_4$, Al$_2$O$_3$, SiO$_2$, and hydroxides.

The powders passivated at pH 8 contain Fe^0 and a small amount of Fe^{3+} (Fig. 4(i)), while the Al spectrum is resolved into Al^{3+} and Al^0 peaks, as shown in Fig. 4(j). Fig. 4(k) shows the Si^{4+} and Si^0 components; the Si 2p peak is shifted slightly to a low binding energy of 101.6 eV for the Si^{4+} with increased pH, which is similar to the findings from a previous investigation [35], indicating a decrement of the Si dissolution rate with increased pH. The O 1s spectrum is fitted with Al^{3+}, Si^{4+}, and OH$^-$ (Fig. 4(l)). Hence, the insulation coating obtained by means of NaNO$_3$ at pH 8 mainly consists of Al$_2$O$_3$, SiO$_2$, and hydroxides.

Fig. 5 displays cross-sectional TEM images of the oxidation layer obtained by means of NaNO$_3$ passivation at pH 2 after annealing. The oxidation layer is indicated by the arrow in Fig. 5(a); it exhibits the characteristics of a bilayer and has a thickness of around (8.6 ± 0.5) nm. The coexistence of crystalline and amorphous regions is evidenced by the SAED pattern taken from the rectangular area indicated in Fig. 5(a) as the insert in Fig. 5(b). The spacing of the rings (2.81 Å, 1 Å = 10^{-10} m) corresponds to AlO(OH) [36,37]. Based on the FTIR and XPS results discussed previously, the diffraction spots may be due to the formation of crystalline Al$_2$O$_3$ via partial decomposition of the AlO(OH) after annealing at 700 °C [38,39]. Fig. 5(c) reveals the coexistence of Fe, Si, Al, and O according to the EDS results for the oxidation layer taken from the rectangular region indicated in the high-angle annular dark-field (HAADF) image. Thus, the coating layer mainly contains Fe$_2$O$_3$, SiO$_2$, Al$_2$O$_3$, and AlO(OH).

Fig. 6(a) shows a cross-sectional TEM image taken from the sample passivated at pH 5. The coating, indicated by the arrow,

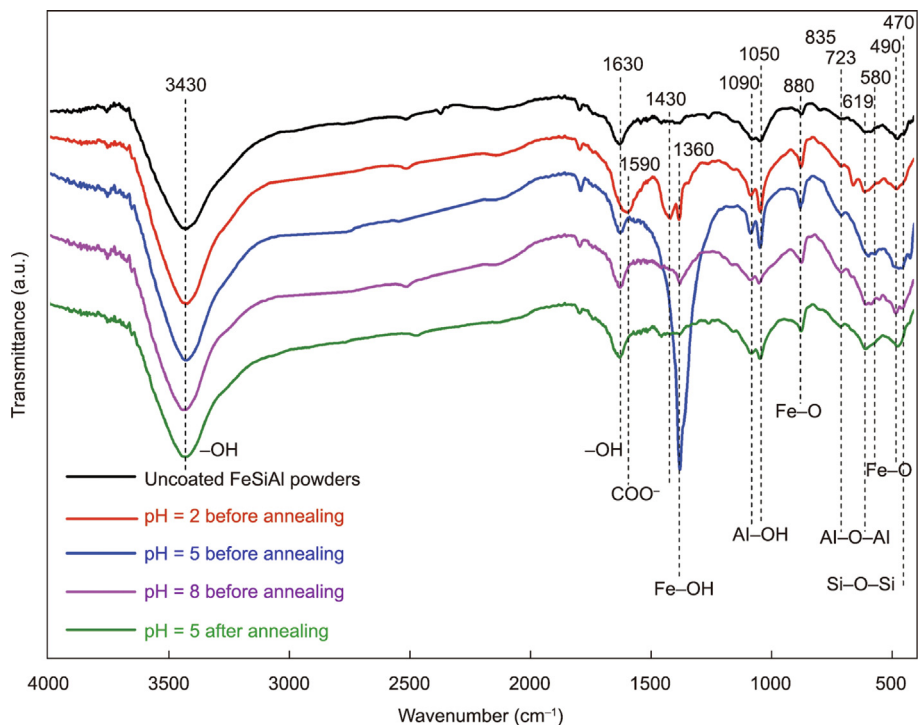**Fig. 3.** FTIR data for uncoated FeSiAl powders and for those passivated with 20 wt% NaNO$_3$ at different pH values.
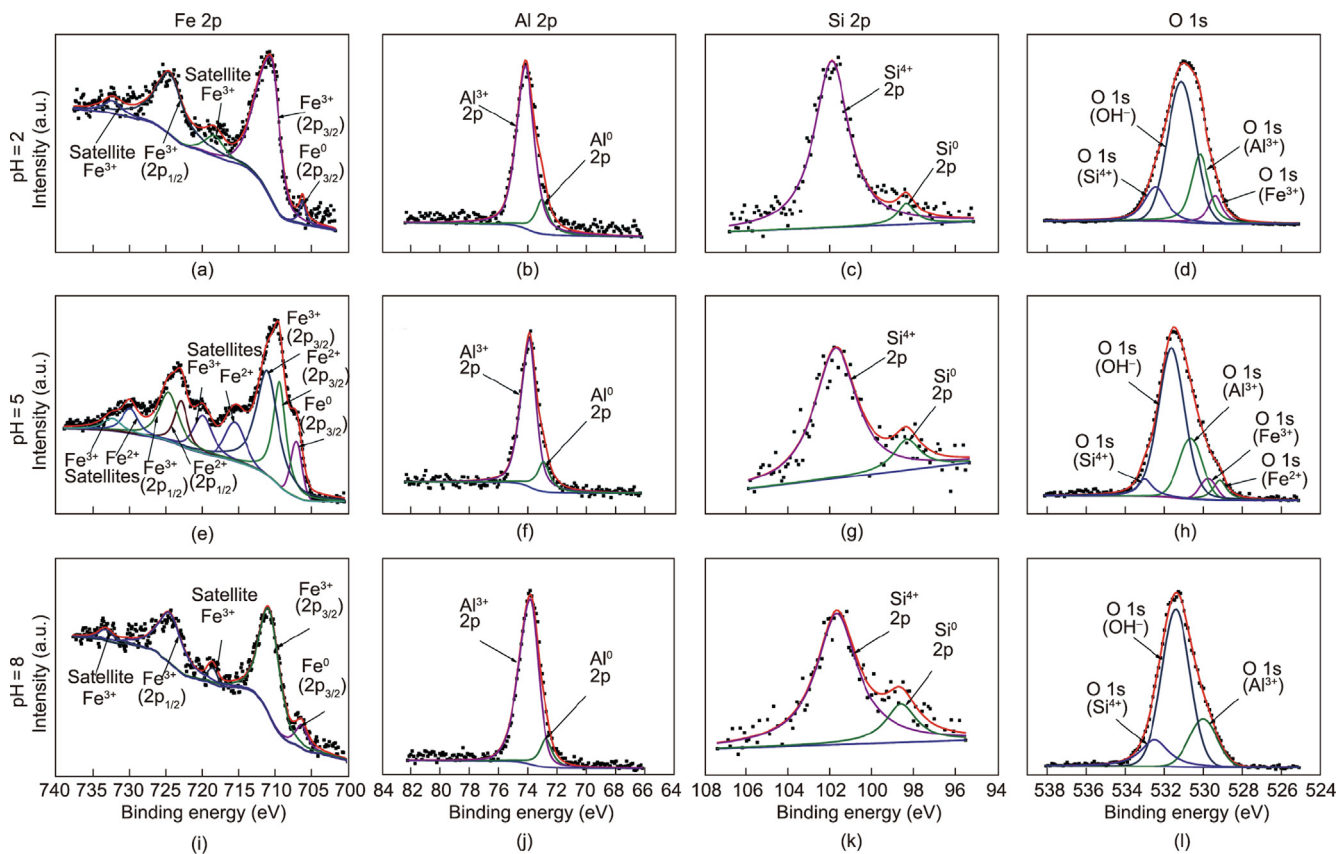

Fig. 4. XPS results illustrating the (a, e, i) Fe 2p, (b, f, j) Al 2p, (c, g, k) Si 2p, and (d, h, l) O 1s peaks for FeSiAl powders passivated by NaNO$_3$ with different pH values of (a–d) 2, (e–h) 5, and (i–l) 8 after annealing.
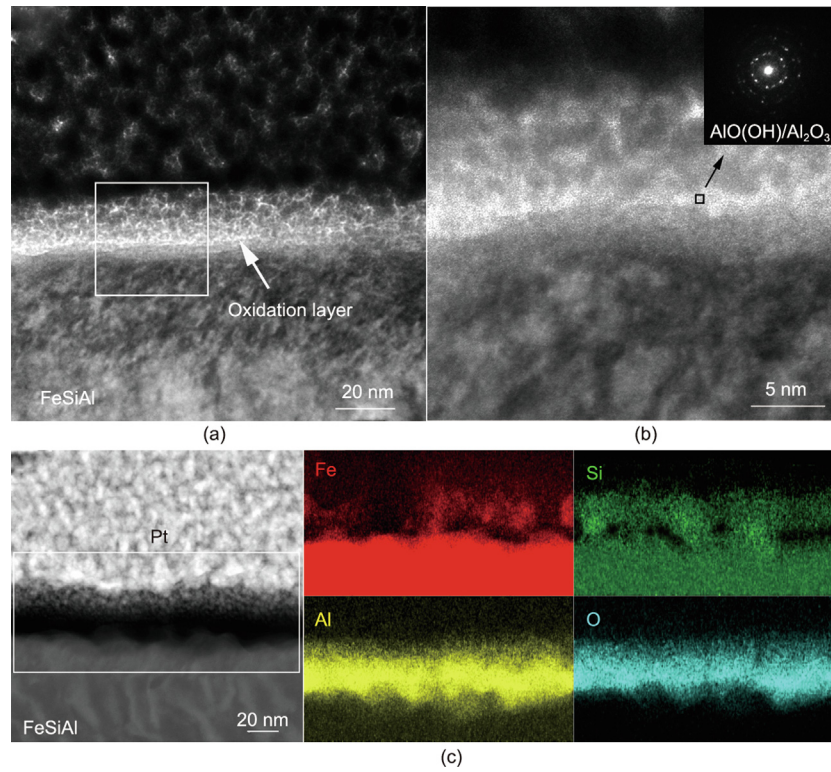
Fig. 5. (a, b) TEM images, with SAED as the inset, of FeSiAl powders subjected to NaNO$_3$ passivation at pH 2 after annealing. (c) High-angle annular dark-field (HAADF) image and EDS results illustrating the Fe, Si, Al, and O distribution.
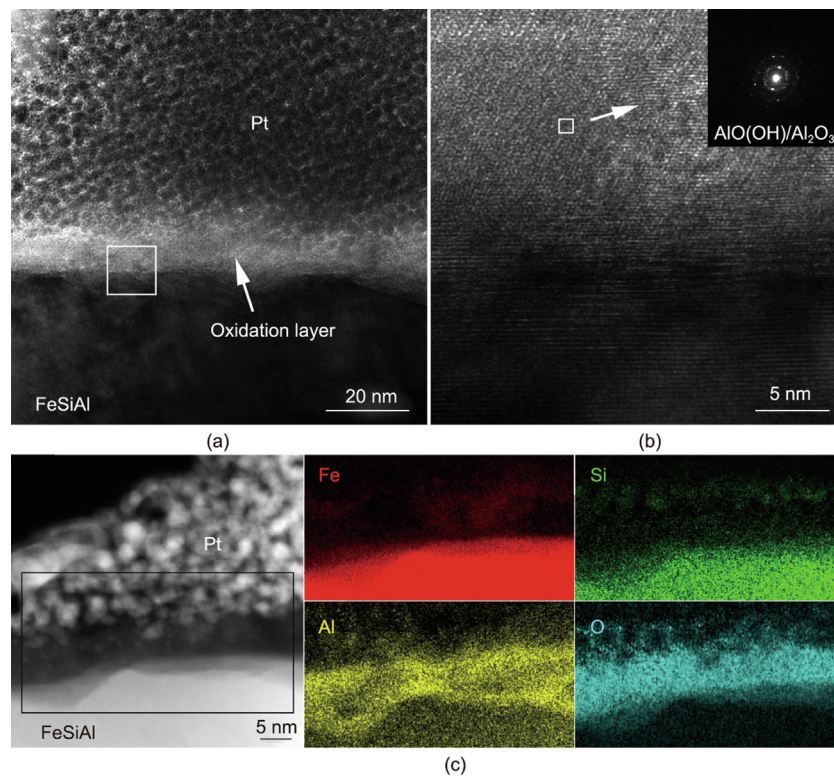

Fig. 6. (a, b) TEM images and SAED pattern of the FeSiAl powders subjected to NaNO$_3$ passivation at pH 5 after annealing. (c) HAADF image and EDS results illustrating the Fe, Si, Al, and O distribution.

exhibits bilayer characteristics with a thickness of around (11.2 ± 0.3) nm. Fig. 6(b) shows that the insulation coating contains amorphous AlO(OH) mixed with crystalline Al_2O_3, according to the inserted SAED pattern, while the HAADF image and EDS mappings in Fig. 6(c) indicate the presence of Al, O, and subtle Fe and Si in the coating layer.
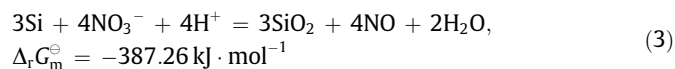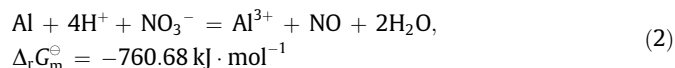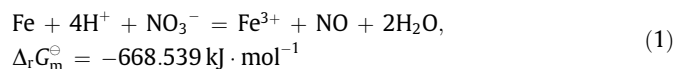
We also investigated the influence of the alkalinity, microstructure, and composition of the insulation coating obtained by $NaNO_3$ passivation at pH 8 after annealing. A wavy interface was observed between the base metal and the coating layer (Fig. 7(a)), with an average thickness of around (6.7 ± 0.8) nm based on measurements of various regions from multiple TEM images. Fig. 7(b) shows the enlarged TEM image and SAED pattern, indicating the coexistence of amorphous AlO(OH) and polycrystalline Al_2O_3. The HAADF image and EDS mappings shown in Fig. 7(c) demonstrate the dominant existence of Al, Si, and O in the insulation coating. Thus, the sample passivated at pH 8 after annealing mainly forms a thin oxidation layer containing Al_2O_3, AlO(OH), and SiO_2.

3.3. Growth mechanism of the insulation coatings

Fig. 8 illustrates the growth model for the bilayer-structured coating on the surface of the FeSiAl powders, which consists of a barrier and a precipitation layer [40]. During passivation, partial Fe, Al, and Si atoms are directly oxidized into Fe_2O_3, Fe_3O_4, Al_2O_3, and SiO_2, forming an inner oxide layer. Cations such as Fe^{3+} and Al^{3+} may transmit through the barrier layer and accumulate at the interface between the barrier layer and the $NaNO_3$ solution to form an outer layer composed of $Fe(OH)_3$ together with $Al(OH)_3$ and AlO(OH) via hydrolytic precipitation.

At pH 2, the barrier layer is formed by the oxidation of the Fe, Al, and Si, following Reactions (1)–(3). Changes in the Gibbs free energy ($\Delta_r G_m^{\ominus}$) were estimated based on the standard entropy $S_m^{\ominus}$

and enthalpy of formation ($\Delta_f H_m^{\ominus}$) [41]. The $\Delta_r G_m^{\ominus}$ is negative for Fe, Al, and Si oxidation, with the strongest reactivity for the Al. As a result of the excessive amount of H^+, hydroxides in the precipitation layer are subjected to dissolution [41,42].

$$Fe + 4H^+ + NO_3^- = Fe^{3+} + NO + 2H_2O,$$
$$\Delta_r G_m^{\ominus} = -668.539 \text{ kJ} \cdot \text{mol}^{-1} \tag{1}$$

$$Al + 4H^+ + NO_3^- = Al^{3+} + NO + 2H_2O,$$
$$\Delta_r G_m^{\ominus} = -760.68 \text{ kJ} \cdot \text{mol}^{-1} \tag{2}$$

$$3Si + 4NO_3^- + 4H^+ = 3SiO_2 + 4NO + 2H_2O,$$
$$\Delta_r G_m^{\ominus} = -387.26 \text{ kJ} \cdot \text{mol}^{-1} \tag{3}$$

The oxidation reactions for Al and Si at pH 5 are similar to those at pH 2. The reaction for Fe however, changes as shown below, since the oxidability of the NO_3^- is reduced with the decrement of H^+, resulting in Fe^{2+} accompanying the Fe^{3+}. In addition, dissolution of the precipitated hydroxides is decreased due to the decreased H^+ concentration.

$$3Fe + 8H^+ + 2NO_3^- = 3Fe^{2+} + 2NO + 4H_2O,$$
$$\Delta_r G_m^{\ominus} = -469.9 \text{ kJ} \cdot \text{mol}^{-1} \tag{4}$$
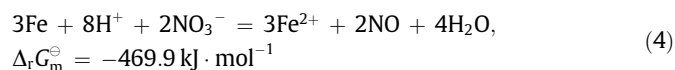
Further increasing the pH to 8 hinders the passivating reactions due to the insufficient oxidability of the NO_3^-. The Fe tends not to be oxidized; moreover, the degrees of Reactions (2) and (3) are reduced. Hydrolysis precipitation may also be slow, with little dissolution. In an alkaline $NaNO_3$ solution, local corrosion may occur on the FeSiAl powder surface (Fig. 2(e)) through the following reaction:
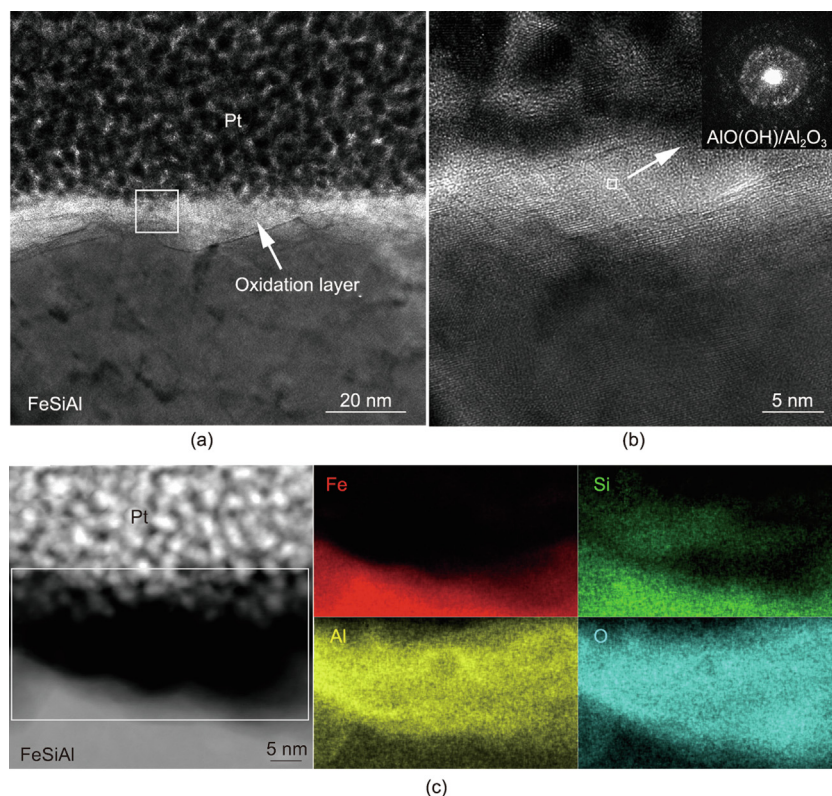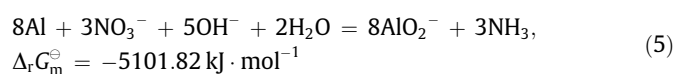
$$8Al + 3NO_3^- + 5OH^- + 2H_2O = 8AlO_2^- + 3NH_3,$$
$$\Delta_r G_m^{\ominus} = -5101.82 \text{ kJ} \cdot \text{mol}^{-1} \tag{5}$$

Fig. 7. (a, b) TEM images and SAED pattern taken from the FeSiAl powders subjected to $NaNO_3$ passivation at pH 8 after annealing. (c) HAADF image and EDS results illustrating the Fe, Si, Al, and O distribution.
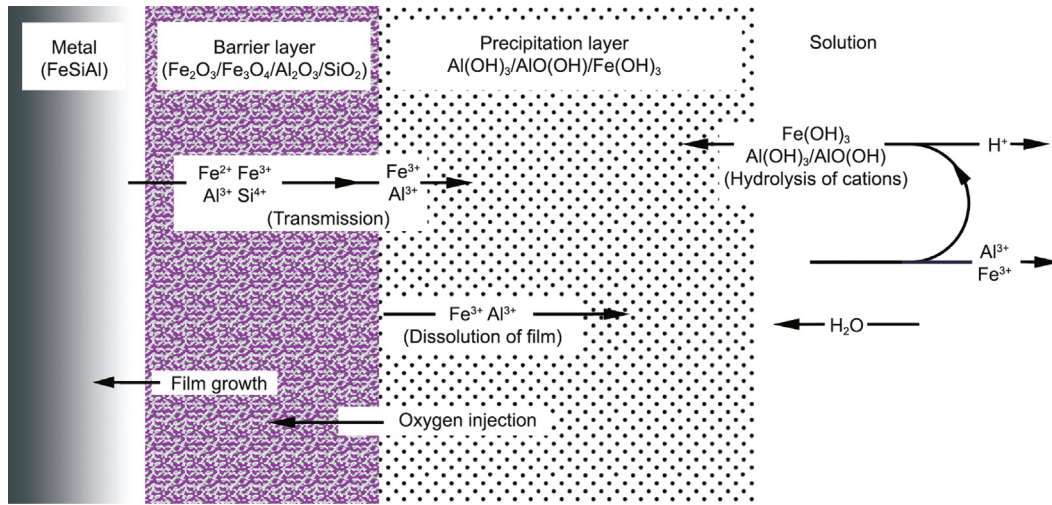
Fig. 8. Schematic growth of the bilayer coating on the surface of the FeSiAl powders.

The kinetics for the formation of the carrier and the participation layer can be understood according to the point defect theory [43]. Reaction (6) at the interface between the metal and the barrier layer is responsible for the barrier layer growth, and its dissolution depends on Reaction (7) at the interface between the barrier layer and the precipitation layer.

$$m \xrightarrow{k} M_M + \frac{\chi}{2} V_O^{\cdot\cdot} + \chi e^- \tag{6}$$

$$MO_{\chi/2} + \chi H^+ \xrightarrow{k'} M^{\delta+} + \frac{\chi}{2} H_2O + (\delta - \chi)e^- \tag{7}$$

where m and M_M are the metal atom and cation, respectively; $V_O^{\cdot\cdot}$ is the oxygen vacancy; $MO_{\chi/2}$ is the stoichiometric barrier layer oxide; χ is the oxidation state of the cation in the barrier layer; $M^{\delta+}$ is the metal cation diffused into the precipitation layer; and k and k' are the rate constants for Reactions (6) and (7), respectively. The change rate of the thickness of the barrier layer can be expressed as follows [40], involving the growth rate and the dissolution rate represented on the right side of the equation.

$$\frac{dL}{dt} = \Omega k - \Omega k' C_{H^+}^n \tag{8}$$

where L is the barrier layer thickness changing over time t; Ω is the barrier layer volume per mole of cation; C_{H^+} is the H^+ concentration; and n is the kinetic order with respect to C_{H^+}. The growth constant k is related to the electrode potential $\varphi_{(NO_3^-/NO)}$ of the reaction between Fe, Al, Si, and NO_3^- during the passivation process [40,43]. The potential can be calculated based on the Nernst equation [41]:

$$\varphi_{(NO_3^-/NO)} = \varphi_{NO_3^-/NO}^{\ominus} + \frac{0.059}{3} \log \frac{C_{NO_3^-} \cdot C_{H^+}^4}{P_{NO}/P^{\ominus}} \tag{9}$$

where $C_{NO_3^-}$ is the NO_3^- concentration, $\varphi_{(NO_3^-/NO)}^{\ominus}$ is the standard electrode potential, P_{NO} is the partial pressure of the NO, and $P^{\ominus}$ is the standard pressure.

Fig. 9 illustrates the evolution of the insulation layer at different pH values. At pH 2, abundant H^+ results in a large $\varphi_{(NO_3^-/NO)}$ for an increased k, giving rise to rapid growth of the barrier layer. The large concentration of H^+ also promotes the conversion of the metal atoms into cations, which are transmitted into the precipitation layer [44], as shown in the growth process in Fig. 9(a), con-

suming a significant amount of the metal atoms in the powder. During dissolution, the high C_{H^+} leads to a high rate of barrier layer dissolution; the excessive H^+ also tends to dissolve the hydroxides, reducing the thickness of the coating. As the pH is increased from 2 to 5, the $\varphi_{(NO_3^-/NO)}$ decreases with reduced H^+ concentration, resulting in a slightly decreased growth rate of the barrier layer and reducing the reaction of metal cations in the hydrolysis precipitation. In addition, dissolution of the bilayer is hindered, resulting in complete insulation with the maximum thickness (Fig. 9(b)). When the pH is further increased to 8, the growth of the barrier and the precipitation layer is slight despite the rather low rate of dissolution, resulting in a significantly reduced coating thickness, as shown in Fig. 9(c).

3.4. Correlating the insulation coating and the magnetic performance

The changes in the performance of the SMCs shown in Fig. 1 can be explained based on the growth mechanisms of the coating layers. Increasing the pH from 2 to 5 results in an increased thickness of the mostly non-magnetic insulation layer that acts as a pinning site, leading to reduced μ_e. At pH 8, the μ_e exhibits poor frequency stability, which can be attributed to the skin effect caused by an increased eddy current [45] due to the formation of a thin and incomplete insulation coating.

The total core loss of the SMCs consists of the hysteresis loss (P_h), the eddy current loss (P_e), and the residual loss (P_r), among which the residual loss is important only at very low induction levels and at very high frequencies and is thus neglectable in this study. Consequently, the P_{cv} can be separated based on the following equation [46]:

$$P_{cv} = P_h + P_e = k_1 f + k_2 f^2 \tag{10}$$

where k_1 and k_2 are the coefficients of the hysteresis loss and the eddy current loss, respectively, and f is the frequency. Fig. 10 shows the contribution of the P_h and P_e of samples prepared at different pH values. The P_h mainly depends on the coercivity, which increases due to the growth of the insulation layer as the pinning sites for domain wall movements as the pH is increased from 2 to 5. The P_h then declines at pH 8 due to incomplete coating. The P_e is determined by the electrical resistivity of the sample, which can be significantly enhanced due to the formation of a sufficient insulation coating at pH 5.
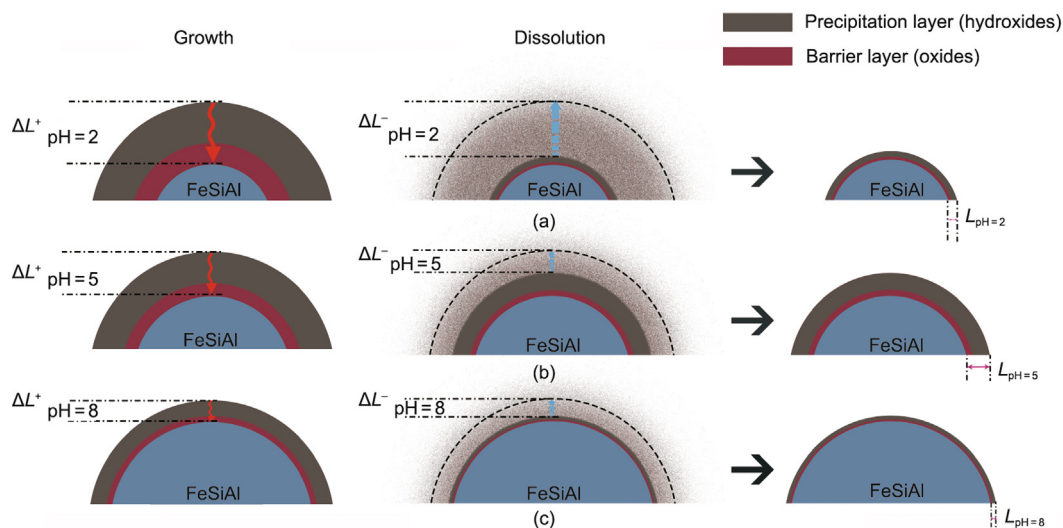
Fig. 9. Schematic illustration showing the growth and dissolution process during the formation of passivation layers at a pH of (a) 2, (b) 5, and (c) 8.
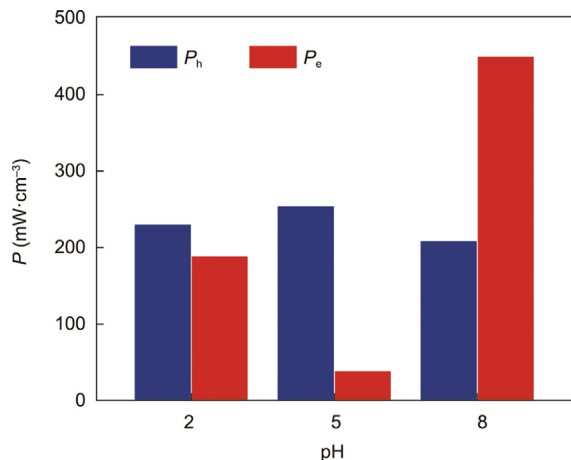

Fig. 10. Separation of the total loss into the hysteresis loss (P_h) and the eddy current loss (P_e) for samples prepared with different pH values.

4. Conclusions

This study reported on the development of NaNO$_3$ passivation as a new insulation coating technology for the fabrication of FeSiAl SMCs. The evolution of the oxidation coatings under different conditions was unveiled using microstructural and compositional analyses of the coatings. The passivation mechanism was revealed by means of a detailed thermodynamic and kinetic analysis. Enhanced magnetic properties (μ_e = 97.2, P_{cv} = 296.4 mW·cm^{-3}) were achieved for the FeSiAl SMCs by optimizing the pH value of the NaNO$_3$ solution. The NaNO$_3$ passivation technology developed here may not only be extendable to other magnetic alloy systems but also open up the possibility to use oxidizing agents such as nitrite, superoxide, and permanganate for advanced insulation coatings.

Acknowledgments

Compliance with ethics guidelines

Mi Yan, Qiming Chen, Dong Liu, Chen Wu, and Jian Wang declare that they have no conflict of interest or financial conflicts to disclose.

Appendix A. Supplementary data

Supplementary data to this article can be found online at https://doi.org/10.1016/j.eng.2022.01.016.

References

[1] Silveyra JM, Ferrara E, Huber DL, Monson TC. Soft magnetic materials for a sustainable and electrified world. Science 2018;362(6413):eaao0195.
[2] Périgo EA, Weidenfeller B, Kollár P, Füzer J. Past, present, and future of soft magnetic composites. Appl Phys Rev 2018;5(3):031301.
[3] Li W, Cai H, Kang Y, Ying Y, Yu J, Zheng J, et al. High permeability and low loss bioinspired soft magnetic composites with nacre-like structure for high frequency applications. Acta Mater 2019;167:267–74.
[4] Talaat A, Suraj MV, Byerly K, Wang A, Wang Y, Lee JK, et al. Review on soft magnetic metal and inorganic oxide nanocomposites for power applications. J Alloys Compd 2021;870:159500.
[5] Hossein Taghvaei A, Ebrahimi A, Gheisari K, Janghorban K. Analysis of the magnetic losses in iron-based soft magnetic composites with MgO insulation produced by sol–gel method. J Magn Magn Mater 2010;322(23):3748–54.
[6] Pang YX, Hodgson SNB, Weglinski B, Gaworska D. Investigations into sol–gel silica and silica hybrid coatings for dielectromagnetic soft magnetic composite applications. J Mater Sci 2006;41(18):5926–36.
[7] Peng Y, Yi Y, Li L, Yi J, Nie J, Bao C. Iron-based soft magnetic composites with Al$_2$O$_3$ insulation coating produced using sol–gel method. Mater Des 2016;109:390–5.
[8] Li L, Chen Q, Gao Z, Ge Y, Yi J. Fe@SiO$_2$@(MnZn)Fe$_2$O$_4$ soft magnetic composites with enhanced permeability and low core loss for high-frequency applications. J Alloys Compd 2019;805:609–16.
[9] Zhao G, Wu C, Yan M. Fabrication and growth mechanism of iron oxide insulation matrix for Fe soft magnetic composites with high permeability and low core loss. J Alloys Compd 2017;710:138–43.
[10] Neamțu BV, Pszola M, Vermeșan H, Stoian G, Grigoraș M, Opriș A, et al. Preparation and characterisation of Fe/Fe$_3$O$_4$ fibres based soft magnetic composites. Ceram Int 2021;47(1):581–9.
[11] Chen Y, Zhang L, Sun H, Chen F, Zhang P, Qu X, et al. Enhanced magnetic properties of iron-based soft magnetic composites with phosphate–polyimide insulating layer. J Alloys Compd 2020;813:152205.
[12] Taghvaei AH, Shokrollahi H, Janghorban K, Abiri H. Eddy current and total power loss separation in the iron–phosphate–polyepoxy soft magnetic composites. Mater Des 2009;30(10):3989–95.
[13] Taghvaei AH, Shokrollahi H, Janghorban K. Properties of iron-based soft magnetic composite with iron phosphate–silane insulation coating. J Alloys Compd 2009;481(1–2):681–6.
[14] Zhang SY, Li SJ, Luo XW, Zhou WF. Mechanism of the significant improvement in corrosion protection by lowering water sorption of the coating. Corros Sci 2000;42(12):2037–41.

[15] Pu H, Jiang F, Yang Z. Studies on preparation and chemical stability of reduced iron particles encapsulated with polysiloxane nano-films. Mater Lett 2006;60 (1):94–7.

[16] Zhao N, He C, Liu J, Gong H, An T, Xu H, et al. Dependence of catalytic properties of Al/Fe$_2$O$_3$ thermites on morphology of Fe$_2$O$_3$ particles in combustion reactions. J Solid State Chem 2014;219:67–73.

[17] Gotić M, Dražić G, Musić S. Hydrothermal synthesis of α-Fe$_2$O$_3$ nanorings with the help of divalent metal cations, Mn^{2+}, Cu^{2+}, Zn^{2+} and Ni^{2+}. J Mol Struct 2011;993(1–3):167–76.

[18] Padmaja P, Anilkumar GM, Mukundan P, Aruldhas G, Warrier KGK. Characterisation of stoichiometric sol–gel mullite by Fourier transform infrared spectroscopy. Int J Inorg Mater 2001;3(7):693–8.

[19] Pang SF, Wu CQ, Zhang QN, Zhang YH. The structural evolution of magnesium acetate complex in aerosols by FTIR–ATR spectra. J Mol Struct 2015;1087:46–50.

[20] Urlaub R, Posset U, Thull R. FT-IR spectroscopic investigations on sol–gel-derived coatings from acid-modified titanium alkoxides. J Non-Cryst Solids 2000;265(3):276–84.

[21] Nasrazadani S. The application of infrared spectroscopy to a study of phosphoric and tannic acids interactions with magnetite (Fe$_3$O$_4$), goethite (α-FeOOH) and lepidocrocite (γ-FeOOH). Corros Sci 1997;39(10–11):1845–59.

[22] Lefèvre G. In situ Fourier-transform infrared spectroscopy studies of inorganic ions adsorption on metal oxides and hydroxides. Adv Colloid Interface Sci 2004;107(2–3):109–23.

[23] Wijnja H, Schulthess CP. ATR–FTIR and DRIFT spectroscopy of carbonate species at the aged γ-Al$_2$O$_3$/water interface. Spectrochim Acta A 1999;55 (4):861–72.

[24] Shen SC, Ng WK, Zhong ZY, Dong YC, Chia L, Tan RBH. Solid-based hydrothermal synthesis and characterization of alumina nanofibers with controllable aspect ratios. J Am Ceram Soc 2009;92(6):1311–6.

[25] Ruhi G, Modi OP, Sinha ASK, Singh IB. Effect of sintering temperatures on corrosion and wear properties of sol–gel alumina coatings on surface pre-treated mild steel. Corros Sci 2008;50(3):639–49.

[26] Duan J, Gregory J. Coagulation by hydrolysing metal salts. Adv Colloid Interface Sci 2003;100–102:475–502.

[27] Nishimura T, Kodama T. Clarification of chemical state for alloying elements in iron rust using a binary-phase potantial–pH diagram and physical analyses. Corros Sci 2003;45(5):1073–84.

[28] Refait P, Génin JMR. The oxidation of ferrous hydroxide in chloride-containing aqueous media and Pourbaix diagrams of green rust one. Corros Sci 1993;34 (5):797–819.

[29] MacDonald DD, Butler P. The thermodynamics of the aluminum–water system at elevated temperatures. Corros Sci 1973;13(4):259–74.

[30] Widdel F, Schnell S, Heising S, Ehrenreich A, Assmus B, Schink B. Ferrous iron oxidation by anoxygenic phototrophic bacteria. Nature 1993;362(6423):834–6.

[31] Yamashita T, Hayes P. Analysis of XPS spectra of Fe^{2+} and Fe^{3+} ions in oxide materials. Appl Surf Sci 2008;254(8):2441–9.

[32] Wannaparhun S, Seal S, Desai V. Surface chemistry of Nextel-720, alumina and Nextel-720/alumina ceramic matrix composite (CMC) using XPS—a tool for nano-spectroscopy. Appl Surf Sci 2002;185(3–4):183–96.

[33] O'Hare LA, Parbhoo B, Leadley SR. Development of a methodology for XPS curve-fitting of the Si 2p core level of siloxane materials. Surf Interface Anal 2004;36(10):1427–34.

[34] Hornetz B, Michel HJ, Halbritter J. ARXPS studies of SiO$_2$–SiC interfaces and oxidation of 6H SiC single crystal Si-(001) and C-(001) surfaces. J Mater Res 1994;9:3088–94.

[35] Duval Y, Mielczarski JA, Pokrovsky OS, Mielczarski E, Ehrhardt JJ. Evidence of the existence of three types of species at the quartz–aqueous solution interface at pH 0–10: XPS surface group quantification and surface complexation modeling. J Phys Chem B 2002;106(11):2937–45.

[36] Friedrich A, Wilson DJ, Haussühl E, Winkler B, Morgenroth W, Refson K, et al. High-pressure properties of diaspore, AlO(OH). Phys Chem Miner 2007;34 (3):145–57.

[37] Bokhimi X, Sánchez-Valente J, Pedraza F. Crystallization of sol–gel boehmite via hydrothermal annealing. J Solid State Chem 2002;166(1):182–90.

[38] Paglia G, Božin ES, Billinge SJL. Fine-scale nanostructure in γ-Al$_2$O$_3$. Chem Mater 2006;18(14):3242–8.

[39] Paglia G, Buckley CE, Rohl AL, Hunter BA, Hart RD, Hanna JV, et al. Tetragonal structure model for boehmite-derived γ-alumina. Phys Rev B 2003;68 (14):144110.

[40] MacDonald DD, Butler P. Passivity—the key to our metals-based civilization. Pure Appl Chem 1999;71(6):951–78.

[41] Dean JA. Lange's handbook of chemistry. 15th ed. Columbus: McGraw-Hill Professional; 1998.

[42] Verdes G, Gout R, Castet S. Thermodynamic properties of the aluminate ion and of bayerite, boehmite, diaspore and gibbsite. Eur J Mineral 1992;4 (4):767–92.

[43] MacDonald DD, Englehardt GR. The point defect model for bi-layer passive films. ECS Trans 2010;28(24):123–44.

[44] MacDonald DD. The history of the point defect model for the passive state: a brief review of film growth aspects. Electrochim Acta 2011;56(4):1761–72.

[45] Wu ZY, Jiang Z, Fan XA, Zhou LJ, Wang WL, Xu K. Facile synthesis of Fe–6.5wt% Si/SiO$_2$ soft magnetic composites as an efficient soft magnetic composite material at medium and high frequencies. J Alloys Compd 2018;742:90–8.

[46] Kollár P, Birčáková Z, Füzer J, Bureš R, Fáberová M. Power loss separation in Fe-based composite materials. J Magn Magn Mater 2013;327:146–50.